

Requirements for fault-tolerant factoring on an atom-optics quantum computer

Simon J. Devitt^{1*}, Ashley M. Stephens¹, William J. Munro^{2,1}, and Kae Nemoto¹
¹*National Institute for Informatics, 2-1-2 Hitotsubashi, Chiyoda-ku, Tokyo 101-8430, Japan and*
²*NTT Basic Research Laboratories, NTT Corporation,*
3-1 Morinosato-Wakamiya, Atsugi, Kanagawa 243-0198, Japan
(Dated: August 20, 2018)

Quantum information processing and its associated technologies has reached an interesting and timely stage in their development where many different experiments have been performed establishing the basic building blocks. The challenge moving forward is to scale up to larger sized quantum machines capable of performing tasks not possible today. This raises a number of interesting questions like: How big will these machines need to be? how many resources will they consume? This needs to be urgently addressed. Here we estimate the resources required to execute Shor's factoring algorithm on a distributed atom-optics quantum computer architecture. We determine the runtime and requisite size of the quantum computer as a function of the problem size and physical error rate. Our results suggest that once experimental accuracy reaches levels below the fault-tolerant threshold, further optimisation of computational performance and resources is largely an issue of how the algorithm and circuits are implemented, rather than the physical quantum hardware.

The prospect of an entirely new industry based on quantum mechanics has motivated technological development and led to a much better understanding of the principals governing our universe at the atomic scale. For quantum technology, experimental progress has been pronounced [1–7]. Not only has a fledgling industry based on quantum key distribution already emerged [8–10] but many experimental groups now routinely demonstrate the ability to create, manipulate and read-out multiple qubits in multiple physical systems with increasingly higher accuracy [11]. The goal of developing a commercially viable, large-scale quantum computer is now coming into view. Theoretical progress is also an essential part, and fault-tolerant quantum error correction techniques, a necessity to deal with imperfect physical components, have been refined substantially [12–14]. The adaptation of these techniques to the physical restrictions of quantum hardware has led to multiple architecture designs, indicating a clear pathway towards future quantum computers [15–23].

While a large-scale quantum computer is still years away, it is now possible to make qualitative and quan-

titative predictions about the performance and required resources of such a computer. Some of the previous predictions consider hardware architectures based on specific physical systems [21, 22, 24–26], which is an essential aspect in resource analysis. However omit a full prescription for executing the algorithms in question. Others consider promising error-correction codes and circuits, such as post-selection [12] and topological error correction [14], yet do so without reference to particular architectures or applications. Above the hardware device level, there are a number of layers of implementation needed to finally run an algorithm. By careful choice of all technological elements and the integration of all layers of implementation, a complete analysis is now possible, which we present in this manuscript.

A full account of the resources required for fault-tolerant quantum computation must consider a number of factors. Each physical component in our computer suffers from errors, therefore an appropriate error correcting code must be chosen to be compatible with the physical restrictions of the hardware. Physical error rates must be suppressed below the fault-tolerant threshold of the chosen code. Next, the code restricts the set of logically encoded gates that can be directly applied to encoded data. Each gate in the high-level quantum algorithm is then decomposed into a universal set of fault-tolerant primitives. To realise these universal primitives, ancillary states and protocols are typically required to enact teleported gates that could otherwise not be directly applied to the encoded data [27–29]. Each of these steps increases the total qubit/time overhead and must be carefully integrated together in a way that all steps are counted.

The precise details of how resources must be calculated depend on the properties of the architecture in question, the techniques utilised for fault-tolerant error correction, and the desired algorithm. In this work we will be utilising a topological error correction code implemented on a large three dimensional cluster state of qubits [14]. This error correction technique, despite the fact that it is the preferred protocol in large scale architectures, has only been briefly studied in regards to *how* a large scale algorithm is implemented. Translating an abstract quantum algorithm into the specific operations needed in the cluster, i.e. the development of a *classical* compiler, has only just begun. This step is anticipated to have a direct impact on the physical resources needed for computation. Typically, estimates consider the number of required gates in the high-level quantum algorithm and the basic amount of ancillary space needed for additional

*electronic address: devitt@nii.ac.jp

fault-tolerant protocols [21, 22, 24]. However these estimates provide only a partial analysis. Error correction codes inevitably suffer from constraints that need to be taken into account: specifically, the interaction of qubits required by the actual algorithm and qubits needed for ancillary fault-tolerant protocols. The scheduling and routing of these ancillary protocols is often overlooked when estimating resources and are likely to dramatically affect resource estimates.

By contrast, compatibility of the topological model to hardware architecture has been demonstrated [20–23]. In our complete analysis, we will employ an atom-optics architecture [20, 30], which is based on the photonic module [31]. The photonic module is a relatively simple device that allows an atomic qubit to mediate the generation of photonics entanglement. The 3D cluster state to support topological error correction will then be created by an array of these devices. Decomposition of each logical gate into a series of physical operations in this architecture is clear, and hence all the geometry and connectivity constraints at the logical and physical level can explicitly be included in the analysis.

The desired algorithm, Shor’s algorithm, is a comparatively simple application compared other problems solvable by a quantum computer [26, 32]. More importantly, it has a rich history of theoretical development and explicit circuit constructions. Hence we can choose an circuit construction amenable to the system design defined above. However, to run the circuit, we still have to take the geometric constraints at the logical level into account. Even though scheduling analysis at the physical level is taken care of by the topological quantum computer model, scheduling and arrangement of gates and ancillary operations within the logical space created by the topological cluster impact performance. This step is largely unexplored, and leaves huge room for optimisation. We should remember that circuit optimisation needs to be done with such restrictions in mind. The ability of an error corrected system to realise the optimal circuit size at the logical-level is dependent on adapting to these constraints, hence estimates should be made with care.

With this given computational system, the number of photonic modules and the time required to execute the algorithm as a function of the problem size and physical error rates desirably characterize the computer. As it is designed, the analysis explicitly deals with all aspects of the error corrected algorithm from the bottom device layer to the top abstract algorithm, giving a unique, but standardized estimation method.

I. PRELIMINARIES

In the topological cluster state model a three-dimensional cluster forms the effective Hilbert space in which computation takes place [14, 33]. The photonic cluster state is continuously prepared from non-entangled

photons by the hardware.

Logical qubits are introduced as pairs of defects in the cluster. Defects are created in the cluster by measuring physical qubits that define the defect in the Z basis [14]. An entangling gate is realised by braiding pairs of defects. Logical errors occur when chains of physical errors connect or encircle defects, which is made less likely by increasing the circumference of defects and by increasing their separation. Physical qubits in the bulk of the cluster, those not associated with defects, are measured in the X basis. This reveals the endpoints of chains of errors, from which the most likely set of errors can be inferred. To estimate physical resources, we are ultimately interested in the size of the three-dimensional cluster state required to execute Shor’s algorithm.

As the algorithm is executed at the logical level, it is useful to introduce a scale factor that essentially encapsulates the overhead associated with error correction [14]. A logical cell is defined as a three-dimensional volume of the cluster that has an edge length of $d + d/4$ unit cells, where d is the distance of the error-correction code. Defects have circumference of d unit cells and are separated by d unit cells [Fig. 1].

A. Shor’s Algorithm

We now turn to the circuit for Shor’s factoring algorithm. There are a number of different circuit implementations of the algorithm [34–37], which assume that arbitrary sets of qubits can be simultaneously entangled without any penalty related to their separation. In the topological model, as gates are realized by braiding defects, one could implement a gate over a long distance without any penalty. However, multiple gates are typically implement at the same time step and necessary

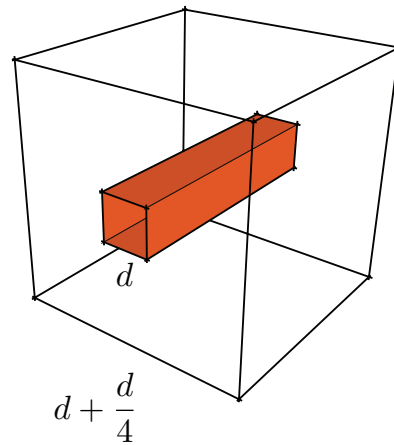


FIG. 1: A logical cell; an error correction independent measure of the size of topological quantum circuits. The lengths are expressed in terms of unit cells of the cluster state. The qubit defect is the coloured region centred within the cell.

scheduling within the topological cluster yields nontrivial overhead.

An easier approach is to modify an existing circuit so that it only requires nearest-neighbour gates in some restricted geometry. This can be done by adding SWAP gates to the circuit [38–40]. The Beauregard circuit [37, 38], which we employ in this manuscript, is a Linear Nearest-Neighbour (LNN) construction [38]. This circuit is not as efficient as others, but its explicit LNN construction means we can apply it directly to the topological cluster without further modification. With logical qubits arranged in a line, the circuit to factor an L -bit number requires $Q = 2L$ qubits and has depth $K = 32L^3$, to the leading order. The circuit is not inherently robust to errors [41], requiring an error rate per gate approximately, $10^{-1}/KQ = 10^{-1}/64L^4$, ensuring a 90% chance of success.

B. Gate decomposition

As with all error corrected models of quantum computation, not all gate operations can be directly applied in a fault-tolerant manner. At the logical level, only preparation of the states $|+\rangle$ and $|0\rangle$, X and Z gates, measurement in the X and Z bases and the CNOT gate can be directly applied. SWAP gates are achieved by deforming the trajectory of the defects with which they are associated. To complete a universal set we add the $R_z(\pi/8)$ and $R_z(\pi/4)$ rotations [14]. To apply these gates we perform a teleported gate using the ancillary states $|A\rangle = (|0\rangle + e^{i\pi/4}|1\rangle)/\sqrt{2}$ and $|Y\rangle = (|0\rangle + i|1\rangle)/\sqrt{2}$. Each time we attempt the $R_z(\pi/8)$ gate, there is a 50% chance that a $R_z(\pi/4)$ correction is required.

To ensure that the error rate of the R_z rotations are sufficiently low, the states $|A\rangle$ and $|Y\rangle$ must be of sufficient fidelity. As these ancillary states are prepared in the cluster via injection protocols [14], state distillation is used to increase the fidelity of the ancilla state [29], consuming multiple $|A\rangle$ or $|Y\rangle$ states with a lower fidelity. This process can be concatenated until the desired fidelity is reached. If p_l is the error probability on the state after l levels of state distillation, then $p_{l+1}^A = 35(p_l^A)^3$ and $p_{l+1}^Y = 7(p_l^Y)^3$ for $|A\rangle$ and $|Y\rangle$ respectively [29]. Each distillation circuit is probabilistic with a failure probability of $O(p)$.

Given our set of logical gates, which now includes the $R_z(\pi/8)$ rotation, we need to decompose the circuit for Shor’s algorithm into a sequence of these fault-tolerantly implemented gates. For an upper bound on the number of gates needed we will (pessimistically) assume every gate is a non-trivial phase rotation that must be approximated by a sequence of logical gates found using the Solovay-Kitaev algorithm [27], and each gate in this sequence is the $R_z(\pi/8)$ rotation, which is most resource intensive amongst our logical gates constituting over 50% of the decomposition [42]. Numerical results suggest that a sequence of $\Lambda = 19.6 \log(1/\epsilon) - 10.5$ gates is required to

achieve an arbitrary single qubit rotation with accuracy ϵ [42]. Hence, to achieve the required error rate, each logical gate in the circuit can be estimated as a sequence of $\Lambda = 19.6 \log(640L^4) - 10.5$ gates.

II. RESULTS

A. Braided circuits

We now translate the decomposed circuit for Shor’s algorithm to a sequence of braids in the three-dimensional cluster state. As each gate in the algorithm is assumed to be a $R_z(\pi/8)$ rotation, this is the logical gate that will be designed. Shown in Fig. 2 is the braiding sequence for the logical $R_z(\pi/8)$ rotation at one and two levels of concatenated state distillation. Full details of these gate constructions are detailed in supplementary material. The braiding sequence is compressed manually into a cuboid such that they can be stacked tightly in the spatial and temporal directions in the cluster. The algorithmic qubits (the ones specified in the Beauregard circuit) are the green defects (two defects per algorithmic qubit occupying a cross sectional area of two logical cells). Immediately above each algorithmic qubit is an empty region of the cluster, this empty space is utilised for braided logic and SWAP gates required by the Beauregard circuit. The linear nearest neighbour design of the original circuit ensures that no further optimisation is required at the algorithmic level and that the defect layout of algorithmic qubits in the cluster is sufficient to realise the depth of the original circuit. Above this empty region is the distillation space for $|Y\rangle$ states, required to implement a $R_z(\pi/4)$ correction gate for each applied $R_z(\pi/8)$ gate and Hadamard operations. Below the algorithmic qubits is the distillation space for $|A\rangle$ states.

At one level of concatenation, each algorithmic qubit has a dedicated $|A\rangle$ and $|Y\rangle$ state distillery. As the algorithmic layer is linear, these distilleries connect from above and below in the cluster (direct connections in the topological model correspond to teleported gates [14]).

For two levels of concatenation the repeating cuboid encapsulates four algorithmic qubits. The first concatenation level has physical injection points for low fidelity $|A\rangle$ and $|Y\rangle$ states and the size of the defects are half of what is required at the algorithmic layer. this reduced size and separation of defects for the first concatenation level is because distillation circuits have a residual error. Therefore if the error of an injected state at the physical level is $O(10^{-3} - 10^{-4})$, then implementing full strength error correction for these circuits is redundant. The residual error from distillation will always dominate. At the second layer of concatenation, the residual error becomes commensurate with the required logical error needed for computation. Therefore, after the first layer of concatenation, defects are expanded and separated to the same size as the required error correction for the algorithm. Additionally, at the second level of concatena-

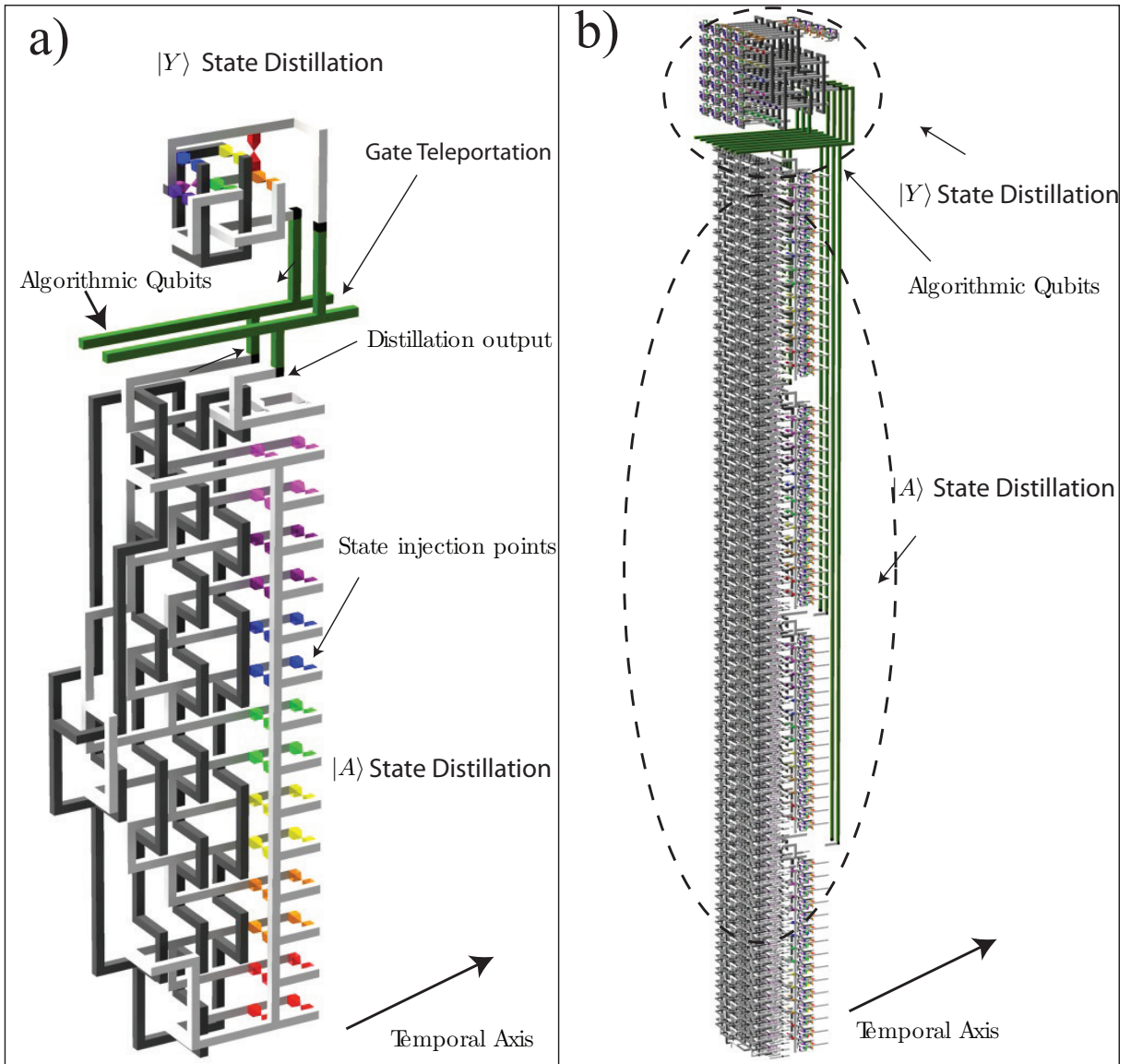


FIG. 2: Explicit braiding constructions for a $R_z(\pi/8)$ rotation in the topological cluster at **a) one** and **b) two** levels of concatenated state distillation. The temporal axis in the cluster is illustrated. For a detailed explanation of these constructions see the supplementary material. Qubits that are part of the algorithmic circuit for Shor are illustrated in green. The cluster volumes and depths for these two circuits are $V = \{210, 1386\}$ and $D = \{5, 9\}$ respectively. Each sequence is designed such they can be stacked together efficiently in either the temporal or spatial directions in the cluster.

tion, the state injection for corrective $|Y\rangle$ states, needed for the $|A\rangle$ state distillation, becomes level one $|Y\rangle$ state circuits, placed in the relevant free space in the cluster.

The application of corrective $R_z(\pi/4)$ rotations for $|A\rangle$ state distillation and the probabilistic nature of the circuits themselves are compensated at the second level of concatenation by utilising free space to add extra distilleries [See supplementary material]. At the first level of concatenation, for $|Y\rangle$ states, there is sufficient space for one extra circuit adjacent to the second level circuit, to compensate for any one failure at level one. For $|A\rangle$ state distillation there is space for two extra circuits within the cuboid to compensate for a given circuit failure. These

circuit failures occur with probability $O(p)$, with p the fidelity of the injected states. Given the extra space for spare level one circuits and assuming p is $O(10^{-3} - 10^{-4})$, we will have too many failures at level one with a probability $O(10^{-5} - 10^{-7})$ for $|Y\rangle$ states and $O(10^{-7} - 10^{-9})$ for $|A\rangle$ states. Therefore, we expect that we will not have sufficient first level states every approximately $10^5 - 10^7$ Logical gates. While these failures result in an increase in circuit depth, they occur infrequently enough to be neglected. Finally, a total of 15 first level circuits for corrective $|Y\rangle$ states, needed by the second level $|A\rangle$ state circuit, are used. The probability that not enough level one $|Y\rangle$ states are available is given by $\frac{15^p}{21^5}$ (i.e. all

problem size. Here we have assumed that $p_{th} = 0.62\%$ [14, 43], $M = 10\text{mm}$ and $T = 10\text{ ns}$ [44]. Contour lines in Figure. 4 indicate where the time to completion is one year, when the total number of photonic modules is 1 billion, and when the cross sectional dimensions are 100m. With an error rate an order of magnitude below p_{th} , the largest problem size that can be completed within a year is $L \approx 820$.

III. DISCUSSION

The current record for factoring general integers is $L = 768$ [45], hence as anticipated, these results show the superiority of quantum computation. However, at the same time, they seem not to demonstrate a significant increase in the processing power of quantum computers.

Our results give a comfortable upper bound for the resource requirements using explicit constructions in the topological model. The time required to factor a 1024-bit number in this analysis is 2.15 years with 1.9 billion photonic modules, required to prepare the cluster. An interesting question to ask here might be how these numbers can be compared with the fundamental circuit used in this analysis. The basic circuit requires a computational depth of $32L^3$ and $2L$ qubits. For physical gate times of 10ns, for $L = 1024$, the error correction overhead is 2.3×10^7 temporally and 9.4×10^5 in terms of qubits/modules. These numbers are based on a physical error rate an order of magnitude below threshold. This overhead, resulting from the error correction, can potentially be significantly reduced by optimisations unrelated to the fundamental hardware. This can be easily highlighted by the fact that decreasing the error rate by an order of magnitude results in a speed-up of to 1.14 years. The same speed-up can be achieved by compactifying the topological circuits shown here by 44% along the temporal axis of the cluster.

There has been many other resource estimates made for a computer employing both concatenated and topological coding models. Thaker *et al.* estimated that to factor a 1024-bit number using an architecture based on trapped ions would take around 25 days [24]. Van Meter *et al.* estimated a 2048-bit number on a distributed architecture based on quantum dots would take around 400 days [21]. Jones *et al.* recently improved the latter estimate to around 10 days [22] by utilising a monolithic array of dots and increasing the speed of fundamental error correction cycles. New results in superconducting designs suggest a factoring time, for a 2000-bit number, slightly less than one day [46]. In these estimates differences arise due to how the algorithm is implemented. Until a complete analysis is performed, it is meaningless to

directly compare them. In particular, more resource efficient techniques are utilised in these results which need to be explicitly integrated within the topological model for future estimates.

All resource estimates, including ours, illustrates that large fraction of the overhead arises from the need to prepare ancillary states. Other results assume sufficient space within the computer such that ancillary protocols can be completed rapidly enough that the depth of the algorithmic circuit is unchanged. This could be of significant benefit. However, the appropriate routing of these ancillary protocols need to be explicit. How distillation circuits are interfaced with data qubits needs to be detailed and exactly which protocols are utilised needs to be analysed. Estimates from Refs. [22, 46] use the most optimal circuit for Shor's algorithm [34, 47]. This circuit has not yet been adapted to the geometric constraints of the topological cluster. Until an appropriate construction is presented for the topological cluster it is difficult to assume that the circuit size will remain unchanged. If such a circuit design is presented, then we anticipate immediate reductions in resources. Previous results also assume that various subcomponents of a fault-tolerant implementation can be applied without space/time penalty. There has been many results published optimising various components in a fully error corrected quantum algorithm [48–51]. However, each of these results have been derived in isolation, some have not been converted into the topological model and none have been carefully integrated together. This is the primary challenge of topological computation. Subcomponents may be efficient, but the success of a large-scale computation requires delicate integration. Our results illustrate that there is a significant gap between optimistic resource estimates and those performed using explicit circuit contractions.

It is clear that before a quantum computer is actually build that algorithmic compilation is a necessity. Reducing the burden on experimental development is ultimately a function of how we realise abstract algorithms. This analysis illustrated that there is much work to be done. While the topological model is promising, its ultimate success is dependant on continual efforts to integrate all necessary protocols in a way that minimises the number of devices and the time required to execute an algorithm.

IV. ACKNOWLEDGEMENTS

We thank N. C. Jones and A. G. Fowler for helpful discussions. This work was partly supported by the Quantum Cybernetics (MEXT) and the FIRST project in Japan.

[1] Gaebel, T. *et al.* Room Temperature coherent control of coupled single spins in solid. *Nature Physics (London)* **2**,

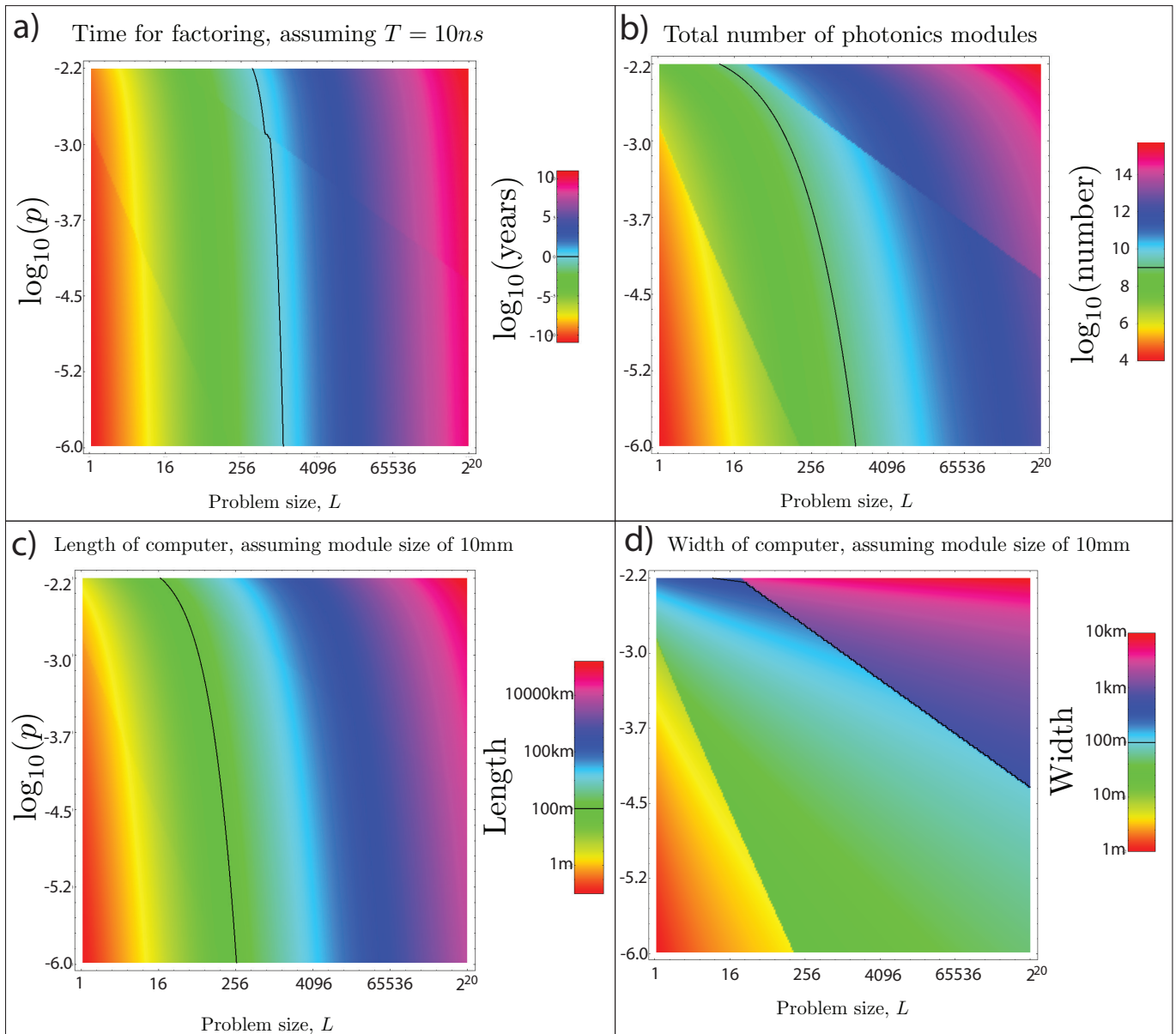


FIG. 4: (a) Time, (b) number of photonic modules and (c), d) computer size required to factor an L -bit number with an error rate p . The discontinuities represent points where the concatenation level for state distillation increases.

- [2] Hanson, R. & Awschalom, D. Coherent manipulation of single spins in semiconductors. *Nature (London)* **453**, 1043–1049 (2008).
- [3] Press, D., Ladd, T. D., Zhang, B. & Yamamoto, Y. Complete quantum control of a single quantum dot spin using ultrafast optical pulses. *Nature (London)* **456**, 218–221 (2008).
- [4] Politi, A., Matthews, J. & O’Brien, J. Shor’s quantum factoring algorithm on a photonic chip. *Science* **325**, 1221 (2009).
- [5] Blatt, R. & Wineland, D. Entangled states of trapped atomic ions. *Nature (London)* **453**, 1008–1015 (2008).
- [6] Pla, J. *et al.* A single-atom electron spin qubit in Silicon. *Nature (London)* **489**, 541–545 (2012).
- [7] Lucero, E. *et al.* Computing prime factors with a Josephson phase qubit quantum processor. *Nature Physics* **8**, 719–723 (2012).
- [8] MagiQ. www.magiqtech.com (2012).
- [9] QuintessenceLabs. <http://qlabsusa.com/> (2012).
- [10] idQuantique. www.idquantique.com (2012).
- [11] Ladd, T. D. *et al.* Quantum Computers. *Nature (London)* **464**, 45–53 (2010).
- [12] Knill, E. Quantum computing with realistically noisy devices. *Nature (London)* **434**, 39–44 (2005).
- [13] Bacon, D. Operator Quantum Error-Correcting Subsystems for self-correcting quantum memories. *Phys. Rev. A* **73**, 012340 (2006).
- [14] Raussendorf, R., Harrington, J. & Goyal, K. Topological fault-tolerance in cluster state quantum computation. *New J. Phys.* **9**, 199 (2007).

- [15] Taylor, J. *et al.* Fault-Tolerant Architecture for Quantum Computation using Electrically controlled Semiconductor Spins. *Nature Physics (London)* **1**, 177–183 (2005).
- [16] Metodi, T., Thaker, D., Cross, A., Chong, F. & Chuang, I. A general purpose architecture layout for arbitrary quantum computations. *Proc. SPIE* **5815**, 91 (2005).
- [17] Hollenberg, L., Greentree, A., Fowler, A. & Wellard, C. Two-Dimensional Architectures for Donor-Based Quantum Computing. *Phys. Rev. B* **74**, 045311 (2006).
- [18] Fowler, A. *et al.* Long-range coupling and scalable architecture for superconducting flux qubits. *Phys. Rev. B* **76**, 174507 (2007).
- [19] Stock, R. & James, D. A Scalable, high-speed measurement based quantum computer using trapped ions. *Phys. Rev. Lett.* **102**, 170501 (2009).
- [20] Devitt, S. *et al.* Architectural design for a topological cluster state quantum computer. *New. J. Phys.* **11**, 083032 (2009).
- [21] Meter, R. V., Ladd, T., Fowler, A. & Yamamoto, Y. Distributed Quantum Computation Architecture Using Semiconductor Nonophotonics. *Int. J. Quant. Inf.* **8**, 295–323 (2010).
- [22] Jones, N. C. *et al.* A Layered Architecture for Quantum Computing Using Quantum Dots. *Phys. Rev. X* **2** (2012).
- [23] Yao, N. *et al.* Scalable Architecture for a Room Temperature Solid-State Quantum Information Processor. *Nature Communications* **3**, 800 (2012).
- [24] Thaker, D., Metodi, T., Cross, A., Chuang, I. & Chong, F. Quantum Memory Hierarchies: Efficient Designs to Match Available Parallelism in Quantum Computing. *International Symposium on Computer Architecture (ISCA-33)*, Boston, MA. 378–390 (2006).
- [25] Steane, A. How to build a 300 bit, 1 Giga-operation quantum computer. *Quant. Inf. Comp.* **7**, 171–183 (2007).
- [26] C.R. Clark, T.S. Metodi, S. & Brown, K. Resource requirements for fault-tolerant quantum simulation: The ground state of the transverse Ising model. *Phys. Rev. A* **79**, 062314 (2009).
- [27] Dawson, C. & Nielsen, M. The Solovay-Kitaev Algorithm. *Quant. Inf. Comp.* **6**, 81–95 (2006).
- [28] Eastin, B. & Knill, E. Restrictions on Transversal Encoded Quantum Gate Sets. *Phys. Rev. Lett.* **102**, 110502 (2009).
- [29] Barrett, S. & Kok, P. Efficient high-fidelity quantum computation using matter qubits and linear optics. *Phys. Rev. A* **71**, 060310(R) (2005).
- [30] Devitt, S., Stephens, A., Munro, W. & Nemoto, K. Integration of highly probabilistic sources into optical quantum architectures: perpetual quantum computation. *New. J. Phys.* **13**, 095001 (2011).
- [31] Devitt, S. *et al.* The Photonic Module: an on-demand resource for photonic entanglement. *Phys. Rev. A* **76**, 052312 (2007).
- [32] Jones, N. C. *et al.* Simulating chemistry efficiently on fault-tolerant quantum computers. *arxiv:1204.0567* (2012).
- [33] Raussendorf, R., Harrington, J. & Goyal, K. A Fault-tolerant one-way quantum computer. *Ann. Phys.* **321**, 2242–2270 (2006).
- [34] Vedral, V., Barenco, A. & Ekert, A. Quantum Networks for elementary arithmetic operations. *Phys. Rev. A* **54**, 147 (1996).
- [35] Gossett, P. Quantum Carry-Save Arithmetic. *quant-ph/9808061* (1998).
- [36] Zalka, C. Fast Versions of Shor’s quantum factoring algorithm. *quant-ph/9806084* (1998).
- [37] Beauregard, S. Circuit for Shor’s algorithm using $2n+3$ qubits. *Quant. Inf. Comp.* **3**, 175–185 (2003).
- [38] Fowler, A., Devitt, S. & Hollenberg, L. Implementation of Shor’s algorithm on a Linear Nearest Neighbour Qubit Array. *Quant. Inf. Comp.* **4**, 237–251 (2004).
- [39] Meter, R. V. & Itoh, K. Fast Quantum Modular Exponentiation. *Phys. Rev. A* **71**, 052320 (2005).
- [40] Kutin, S. Shor’s algorithm on a nearest-neighbor machine. *quant-ph/0609001* (2006).
- [41] Devitt, S., Fowler, A. & Hollenberg, L. Robustness of Shor’s Algorithm. *Quant. Inf. Comp.* **6**, 616–629 (2006).
- [42] Fowler, A. Constructing arbitrary single-qubit Fault-Tolerant gates. *Quant. Inf. Comp.* **11**, 867–873 (2011).
- [43] Barrett, S. & Stace, T. Fault-Tolerant quantum computation with very high threshold for loss errors. *Phys. Rev. Lett.* **105**, 200502 (2010).
- [44] Su, C.-H., Greentree, A., Munro, W., Nemoto, K. & Hollenberg, L. High Speed quantum gates with cavity quantum electrodynamics. *Phys. Rev. A* **78**, 062336 (2008).
- [45] Kleinjung, T. *et al.* Factorization of a 768-bit RSA Modulus. *Proceedings of the 30th annual conference on Advances in cryptology. CRYPTO’10* (2010).
- [46] Fowler, A., Mariantoni, M., Martinis, J. & Cleland, A. Surface Codes, Towards practical large-scale quantum computation. *Phys. Rev. A* **86**, 032324 (2012).
- [47] Cuccaro, S., Draper, T., Kutin, S. & Moulton, D. A new quantum ripple-carry addition circuit. *quant-ph/0410184* (2004).
- [48] Fowler, A. & Devitt, S. A bridge to lower overhead quantum computation. *arxiv:1209.0510* (2012).
- [49] Fowler, A. Time-optimal quantum computation. *arxiv:1210.4626* (2012).
- [50] Jones, N. C. Multilevel distillation of magic states for quantum computing. *arxiv:1210.3388* (2012).
- [51] Bravyi, S. & Haah, J. Magic state distillation with low overhead. *arxiv:1209.2426* (2012).

V. APPENDIX

Here we detail the component constructions required to build a logical $R_z(\pi/8)$ gate, which forms the basis for the resource estimates illustrated in the main text. The goal of these braid constructions is to minimise the total logical volume to implement the fault-tolerant gate and to ensure that braids are constructed in a manner compatible with the underlying circuits and in such a way that they can be packed densely within the overall topological cluster. The techniques used in this section to achieve compact braiding utilises results from Ref. [14] and Ref. [48].

A. Primitive operations

First let us introduce the primitive fault-tolerant operations that are allowed in the topological model. We introduce five types of gates; measurement, initialisation,

state injection, the two-qubit CNOT and the teleported phase rotation, $R_z(\theta)$, $\theta = \{\frac{\pi}{4}, \frac{\pi}{8}\}$. These are illustrated in Fig. 5.

VI. COMPACTIFIED DISTILLATION CIRCUITS

With these primitive operations, the standard circuits for $|A\rangle$ and $|Y\rangle$ state distillation can be converted to a compactified braiding sequence. Shown in Fig. 6 are the canonical circuits for distillation. For the $|Y\rangle$ state, one half of a logical Bell pair is encoded with the $[[7, 1, 3]]$ error correcting code, after which a transversal $R_z(\pi/4)$ gate is applied to the encoded half and measured in the X basis. For $|A\rangle$ state distillation half of the Bell pair is encoded with the $[[15, 1, 3]]$ Reed-Muller code and a transversal $R_z(\pi/8)$ gate applied prior to logical measurement. Given the correct set of measurement results a purified copy of the $|Y\rangle$ or $|A\rangle$ state is teleported to the output half of the original Bell state. In Ref. [48] it was shown how the canonical versions of the braided logic can be compactified using previously known techniques and a process known as defect bridging. Illustrated in Fig. 7 are the compactified versions of the circuits shown in Fig. 6. In Fig. 7a) we show the compactified version of the $|A\rangle$ state distillation circuit. The sets of coloured pyramids represent the injection and gate teleportation needed to realise the transversal $R_z(\pi/8)$ and corrective $R_z(\pi/4)$ gates applied to the encoded half of the initial Bell state, with colour coding matching Fig. 6. Imbedded within the defect structure is the logical Z measurement present in the teleported gate circuit and this logical measurement result dictates if a further corrective $R_z(\pi/4)$ rotation needs to be applied (again via injection and teleportation, this time using a $|Y\rangle$ state). For this circuit, a strictly enforced temporal axis is needed because the logical measurement of the first injection and teleportation dictates if the second one needs to be applied.

In Fig. 7b) and c) we show the compactified version of the $|Y\rangle$ state distillation circuit. Fig. 7b) illustrates the compact version, using known techniques *excluding* bridging, while Fig. 7c) illustrates the final version after defect bridging. We present both circuits as they will both be used in a concatenated distillation sequence. Unlike the $|A\rangle$ state distillation circuits, there is no strict enforcement of a temporal axis in the cluster. Although the transversal $R_z(\pi/4)$ operation for $|Y\rangle$ state distillation is also probabilistic for each teleported gate, the correction operation is a simple Z gate which can be applied via appropriate classical tracking of the Pauli frame. In all three versions of the circuit, the relevant output defects are shown with black caps.

VII. LEVEL 1 CONCATONATED GATE

The level one concatenated $R_z(\pi/8)$ gate is relatively simple to construct, primarily because all injection points correspond to physical qubits in the topological cluster. For each algorithmic qubit in the computer, the region below is devoted to $|A\rangle$ state distillation while one logical cell above contains empty cluster to enable SWAP and CNOT operations between algorithmic qubits. The region above this layer is devoted to $|Y\rangle$ state distillation. Unlike higher levels of concatenation, a single $R_z(\pi/8)$ gate can be defined which can be repeated along the spatial and temporal axes of the cluster. Fig. 8a) illustrates the complete gate which has a depth along the temporal axis of $D = 5$ and a cross sectional area in the cluster of $A = 21 \times 2$. The algorithmic qubit is idle until the distillation operations are complete and with a 50% probability, the corrective $R_z(\pi/4)$ gate need not be applied. At one level of concatenation, all defects in the circuit have the same size and separation. For a level one concatenated circuit there is no extra space for distillation circuits to compensate for a failure event in the circuit itself. As the *logical* error rate required by the computer at one level of concatenation is high (for an experimentally feasible physical gate error), the total number of gates per logical time step will be quite comparatively small and hence the probability of a failed distillation circuit *per logical time step* is quite low. Therefore, in the event that a distillation circuit fails, this structure would be repeated. In our analysis we assume that all gates are $R_z(\pi/8)$ rotations, however in reality this is not the case. In the event of an occasional failure, a repeated distillation circuit can be performed in cluster spaces otherwise vacant due to other logic operations during computation.

VIII. LEVEL 2 CONCATONATED GATE

Forming a second level concatenated $R_z(\pi/8)$ gate is significantly more complex. This is due to injection points at the second level coming from outputs of level one circuits. From Fig. 6a) you can see that accessibility to the $|A\rangle$ state injection points within the braiding structure is quite limited. As a well defined temporal axis has to be maintained, we need to modify the $|A\rangle$ state circuit such that these injection points can be connected easily to the level one outputs. The following sequence of images illustrates the deformations.

These deformations allow us to access the 15 injection points that will use the output from the level one distillation circuits. Note that the temporal axis of the circuit is still well defined as the injection points for the corrective $R_z(\pi/4)$ gates occur after the transversal $R_z(\pi/8)$ gates.

We can now combine the structure in Fig. 13 with 15 copies of level one distillation circuits. As noted in the main text and introduced in Ref. [48], because of the residual error associated with distillation, the error correction associated with level one does not have to be

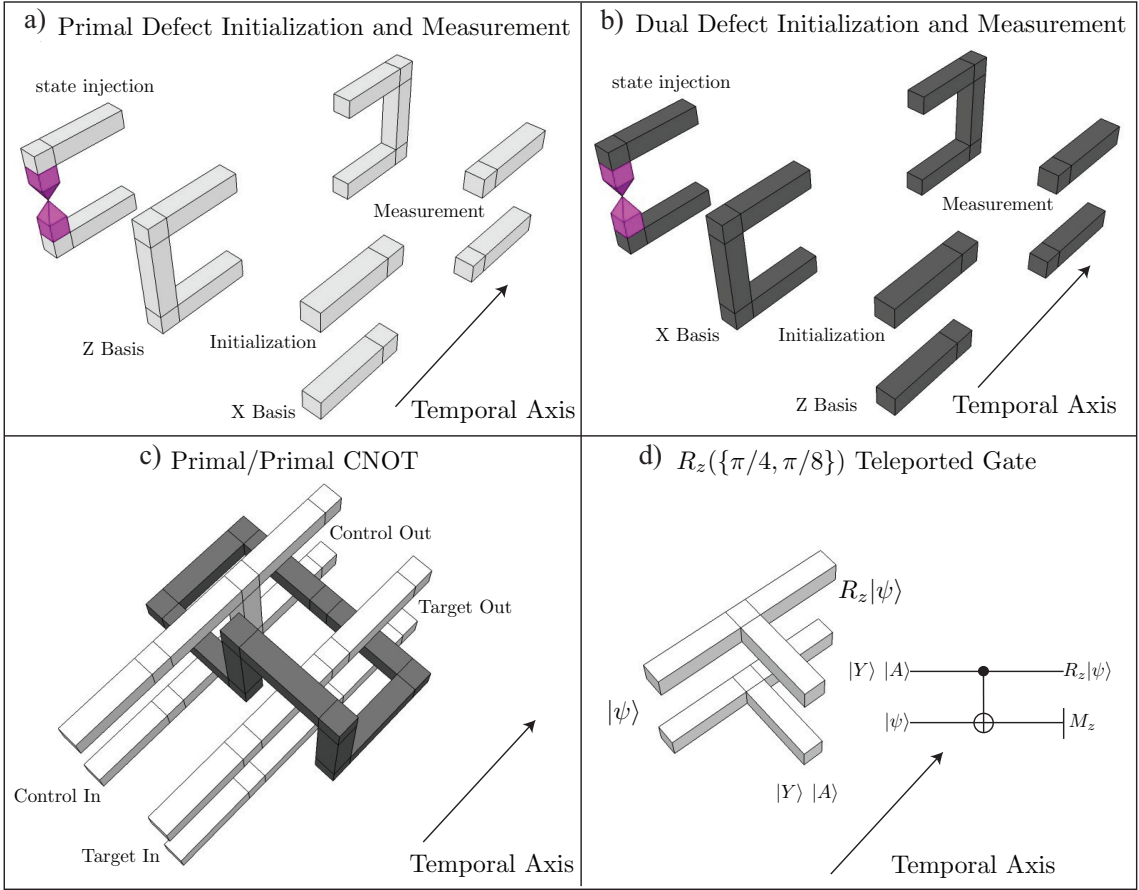


FIG. 5: Examples of basic operations that are used to construct braid sequences. **a)** Primal defects in a horseshoe shape are used to prepare a logical qubit in the state $|0\rangle$ and to measure a logical qubit in the Z basis. An arbitrary state can be prepared by measuring one of the physical qubits (shown in pink) in a rotated basis as the defects are created. **b)** Similarly, dual defects in a horseshoe shape are used to prepare a logical qubit in the state $|+\rangle$ and to measure a logical qubit in the X basis. **c)** A CNOT gate can be achieved by braiding a pair of dual defects (prepared in the state $|+\rangle$) with three pairs of primal defects (the control qubit, the target qubit and an extra qubit prepared in the state $|0\rangle$) [14]. **d)** A teleported Z rotation can be achieved by attaching the relevant ancillary state to the data qubit [14].

as strong as level two. The size and separation of defects at level two must match up with the error correction strength at the algorithmic level, however the strength of error correction for the level one distillation circuits only needs to be as strong as the residual error associated with the circuits themselves. Hence at level one we reduce the size and separation of defects by a factor of two. This reduction in required error correction at level one allows us to stack 17 copies of Fig. 6a) along the input edge of Fig. 13 and form the appropriate input/output connections. The fact that there is space to stack 17 copies of the level one distillation circuit helps us to protect against distillation failure at level one. The failure of the first level to produce enough states requires three distillation circuits to fail, which occurs with a probability of order $\binom{17}{3}p^3$, which for $p = 10^{-3}$ is $O(10^{-7})$. Therefore, a failure at the first level of concatenation will not occur at every logical time step and only in certain rare times will an algorithmic qubit have to wait until a level one distillation circuit is redone.

After defects are outputted from the level one circuits they are expanded to full error correction strength and attached to the level two circuit at the appropriate points (in Fig. 15 we have removed the pyramid structures at the injection points of the level two circuit, but retain the colour coding). This expansion needs to be done carefully. While the level one circuit can have a separation between defects half that of the level two circuit, the separation of level one defects and level two defects *must* be the same as separations within the level two circuit. This is because error chains can begin on a level two defect and terminate on a level one defect.

The final part of this circuit is the corrective $R_z(\pi/4)$ operations that may need to be applied at the second level of concatenation. Unlike level one circuits, these gates need to utilise $|Y\rangle$ states that have been distilled to level one. Given the compact nature of the level one $|Y\rangle$ state circuits [Fig. 6c)], there is sufficient space adjacent to the relevant injection points to place 15 circuits, one for each possible $R_z(\pi/4)$ corrections of the second

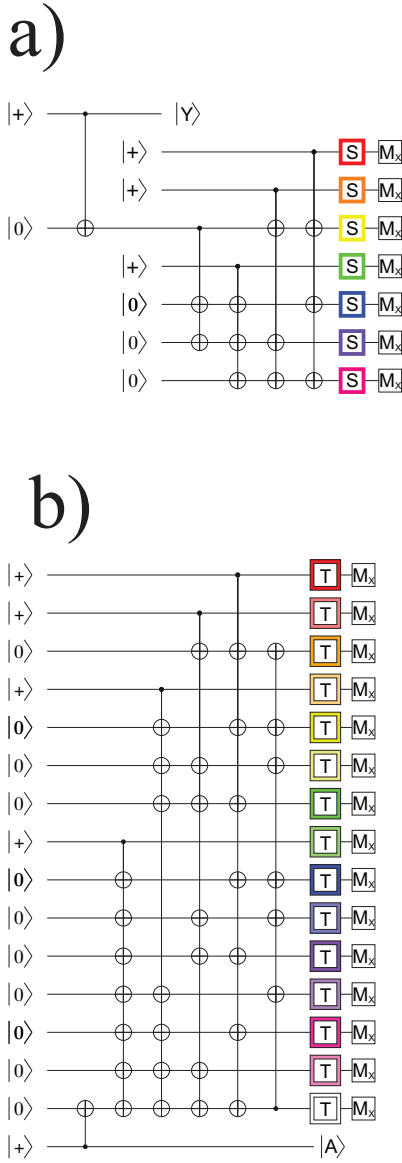


FIG. 6: Quantum circuits required for distillation of the states a) $|Y\rangle$ and b) $|A\rangle$. The coloured boxes represent where error prone states are injected into the cluster. This solar coding corresponds to the coloured injection points in braiding diagrams throughout this paper.

level $|A\rangle$ state circuit, Fig. 16 illustrates. The connection points of each output of the level one $|Y\rangle$ state distillation is expanded to the appropriate separation and size before being joined onto the level two circuit for $|A\rangle$ state distillation. As with level one distillation circuits for $|A\rangle$ states, the distillation circuits for corrective $R_z(\pi/4)$ states can fail. With this defect arrangement, the leading order failure channel is when a single $|Y\rangle$ state circuit fails **and** all 15 correction gates need to be applied. This probability is given by, $\frac{15p}{2^{15}}$, which for $p = O(10^{-3})$ is $O(10^{-7})$, again ensuring that additional time will only be needed in the computer every $O(10^7)$ logical gates.

The braiding structure of Fig. 16 now allows for the application of an encoded $R_z(\pi/8)$ gate at two levels of concatenated distillation, but there are still two more things to consider. While we have introduced 15 copies of level one $|Y\rangle$ state distillation for the correction of the second level $|A\rangle$ state circuit, we still require a level two distilled $|Y\rangle$ state in order to apply a possible correction gate to the final $R_z(\pi/4)$ rotation. As with the level one $R_z(\pi/8)$ gate, this distillation is performed above the algorithmic layer in the cluster.

The second level distillation circuit for $|Y\rangle$ states is shown in Fig. 14. Note that we have used two different circuits for level one distillation [Fig. 6c)] and level two [Fig. 6b)]. We have not attempted to perform further compression of the level two circuit manually as its volume is sufficiently small as to not impact the depth of the overall $R_z(\pi/8)$ gate.

This circuit can now be incorporated into the larger structure, with the appropriate SWAP space left between the algorithmic layer and the $|Y\rangle$ state distillation layer. Along with the second level $|Y\rangle$ state distillation circuit, we have illustrated where an additional first level circuit can be placed in order to compensate for the possibility that one of the seven, first level circuits fail. These failure are also compensated by the fact that the final second level $|Y\rangle$ states are only needed 50% of the time. Hence this circuit element, utilised every time a $R_z(\pi/8)$ gate is applied, over supplies distilled $|Y\rangle$ states.

From Fig. 17, the last issue to solve should be clear. The space utilised for $|A\rangle$ state distillation occupies a cross sectional space in the lattice equal to four algorithmic qubits. Therefore, we need to duplicate the distillation structure vertically in order to produce sufficient states to serve these four algorithmic qubits. Stacking three additional copies of the $|A\rangle$ state distillation circuits below the one in Fig. 17 gives us the stackable braiding sequence which enacts $R_z(\pi/8)$ gates over four algorithmic qubits. This leads to the final structure illustrated in the main text.

Implicit in these images (and throughout the discussion) is the possibility of dynamical configuration of these structures if level one distillation circuits fail. These diagrams assume that all distillation circuits output successfully and can be connected as shown. If this is not the case, a reconfiguration of the overall circuit is needed. The design of these reconfigured circuits can be done offline, but their actual application will be chosen dynamically as the computation is run. As discussed, we have given sufficient space within the second level structure to ensure that a total failure (i.e. one where we do not have sufficient distilled states at the first level of concatenation) does not occur at every time step of computation. However, it is expected that at least *one* circuit will fail throughout the computer, at every logical time step, that *can* be compensated by these extra resources. The dynamical reconfiguration is not expected to increase the depth of these fault-tolerant gates in a significant way, but do still need to be calculated. Given the large num-

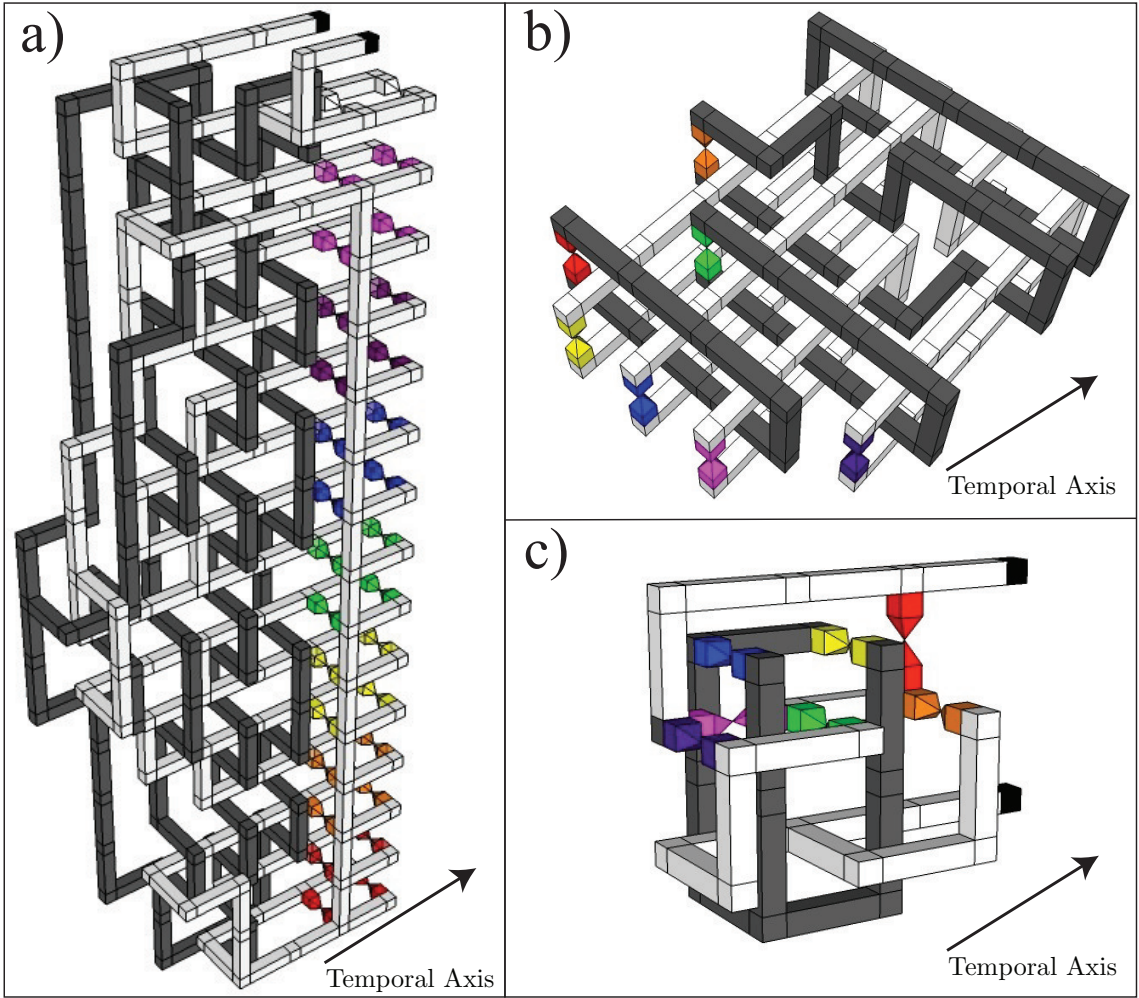


FIG. 7: Braiding diagrams for **a)** $|A\rangle$ state distillation and **b), c)** $|Y\rangle$ state distillation. These compactified circuits are from Ref. [48]. We illustrate two designs for $|Y\rangle$ state distillation as the circuit in Fig. B) will be utilised at the second concatenation level. Coloured pyramid structures represent state injection points to implement the $R_z(\pi/4)$ and $R_z(\pi/8)$ gates needed in the distillation circuits.

ber of possible failure points the specification of all possible configurations will need to be done in an automated manner and is the focus of future work.

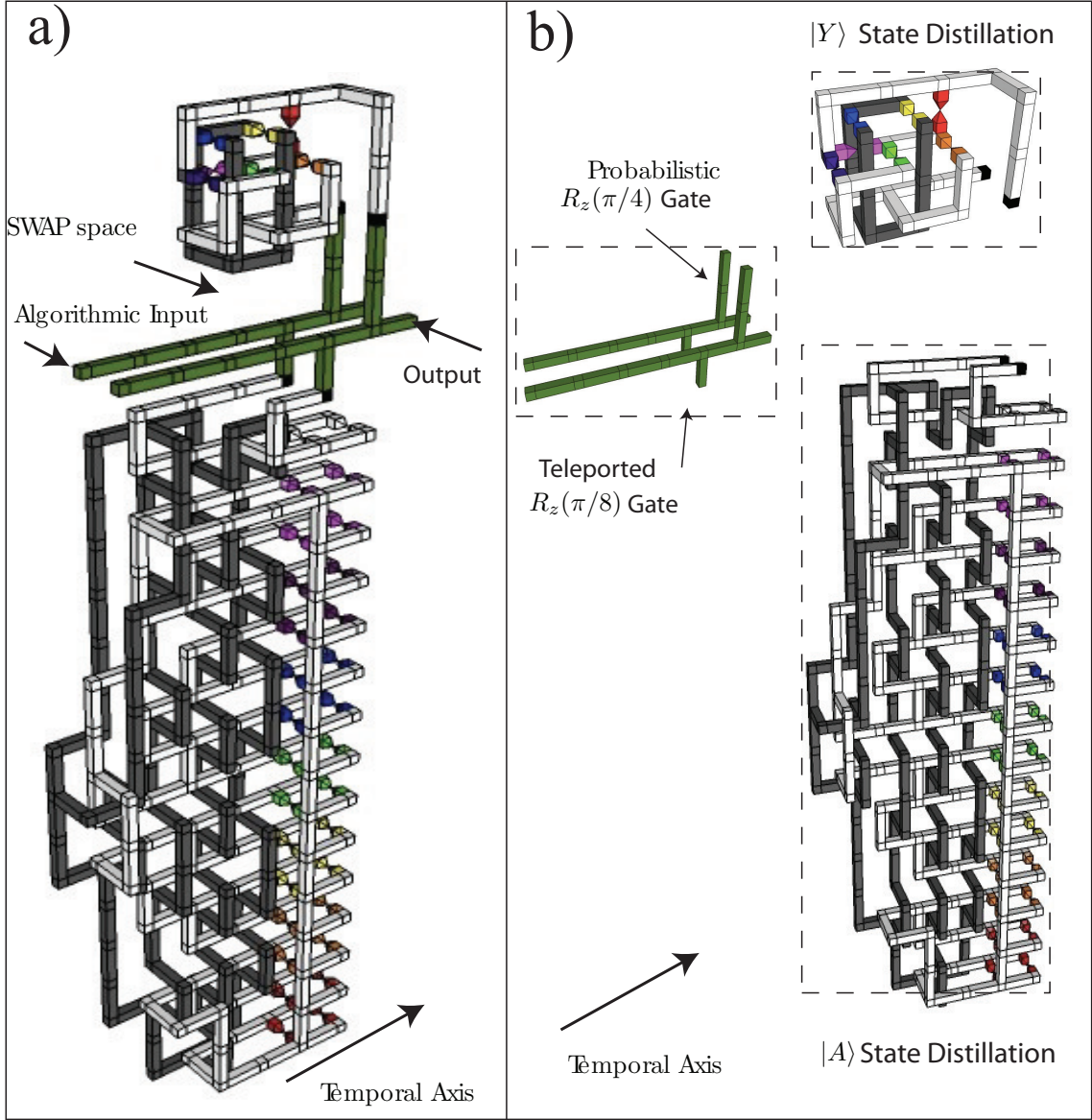


FIG. 8: $R_z(\pi/8)$ gate at one level of concatenated distillation. Fig. **A**) shows the connected circuit, including $|A\rangle$ state distillation, $|Y\rangle$ state distillation for the corrective $R_z(\pi/4)$ operation and the (green) algorithmic qubit. Fig. **B**) illustrates each of the three components. The temporal axis through the cluster is illustrated.

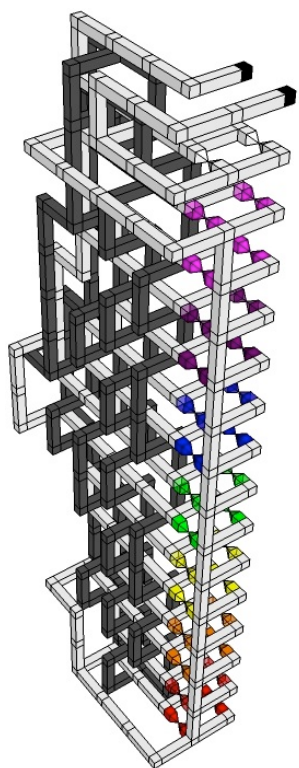


FIG. 9: The circuit from Fig. 6a) is rotated 90 degrees around the injection points. This opens access to these junctions from the input side. Three injection points (White, translucent pink and red) remain difficult to access due to primal defects.

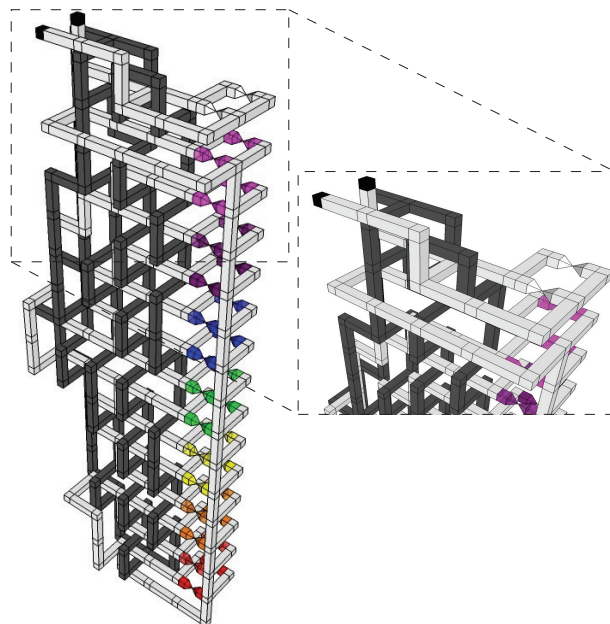


FIG. 11: The output defects are rotated 180 degrees and moved to the left.

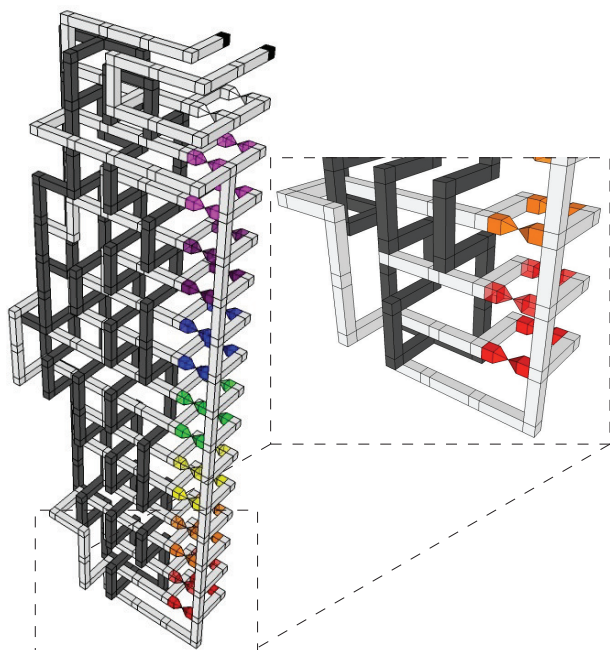


FIG. 10: The primal defect strand near the red injection point is rotated, giving input access to the injection point

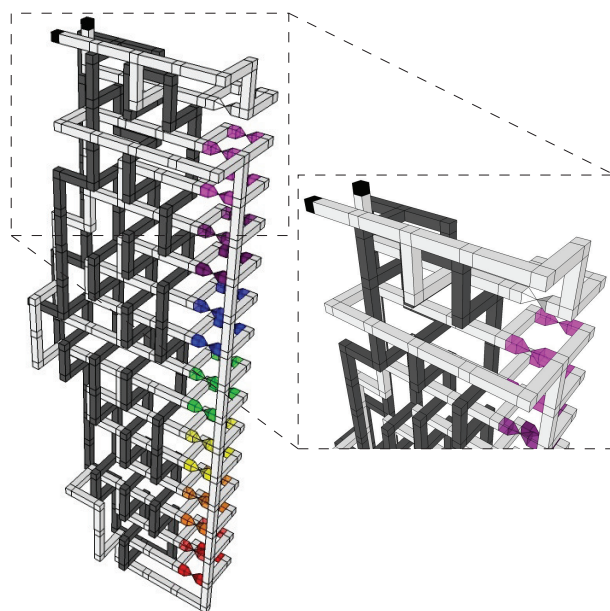


FIG. 12: Primal defect connecting to output is raised to give access to the white injection point.

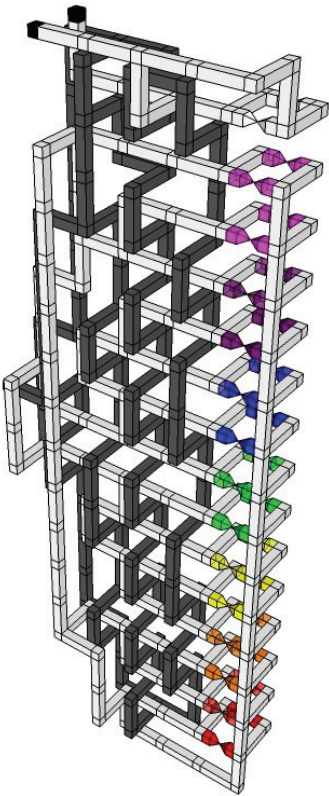


FIG. 13: The primal defect strand blocking access to the translucent pink injection point is deformed along the rightmost primal defect strand creating and then further deformed to the left. This gives access to the injection point from the input side.

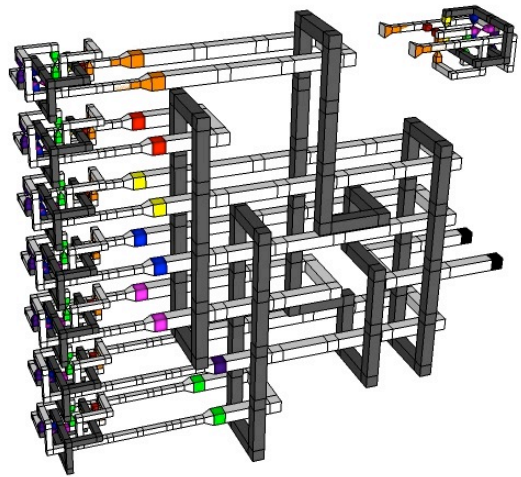


FIG. 14: Second level distillation circuit for $|Y\rangle$ states. In order to have clean access to the seven injection points at level two, a less optimised version of the circuit is used. This structure does have the ability to be compressed further, however the majority of resources needed by the $R_z(\pi/8)$ gate is dedicated to $|A\rangle$ state distillation and consequently we do not compact this circuit further. Space in the structure also exists for an additional level one distillation circuit to protect against circuit failure at level one. This circuit can connect without penalty by a reordering of qubits in the second level circuit and connecting the auxiliary circuit to the output side.

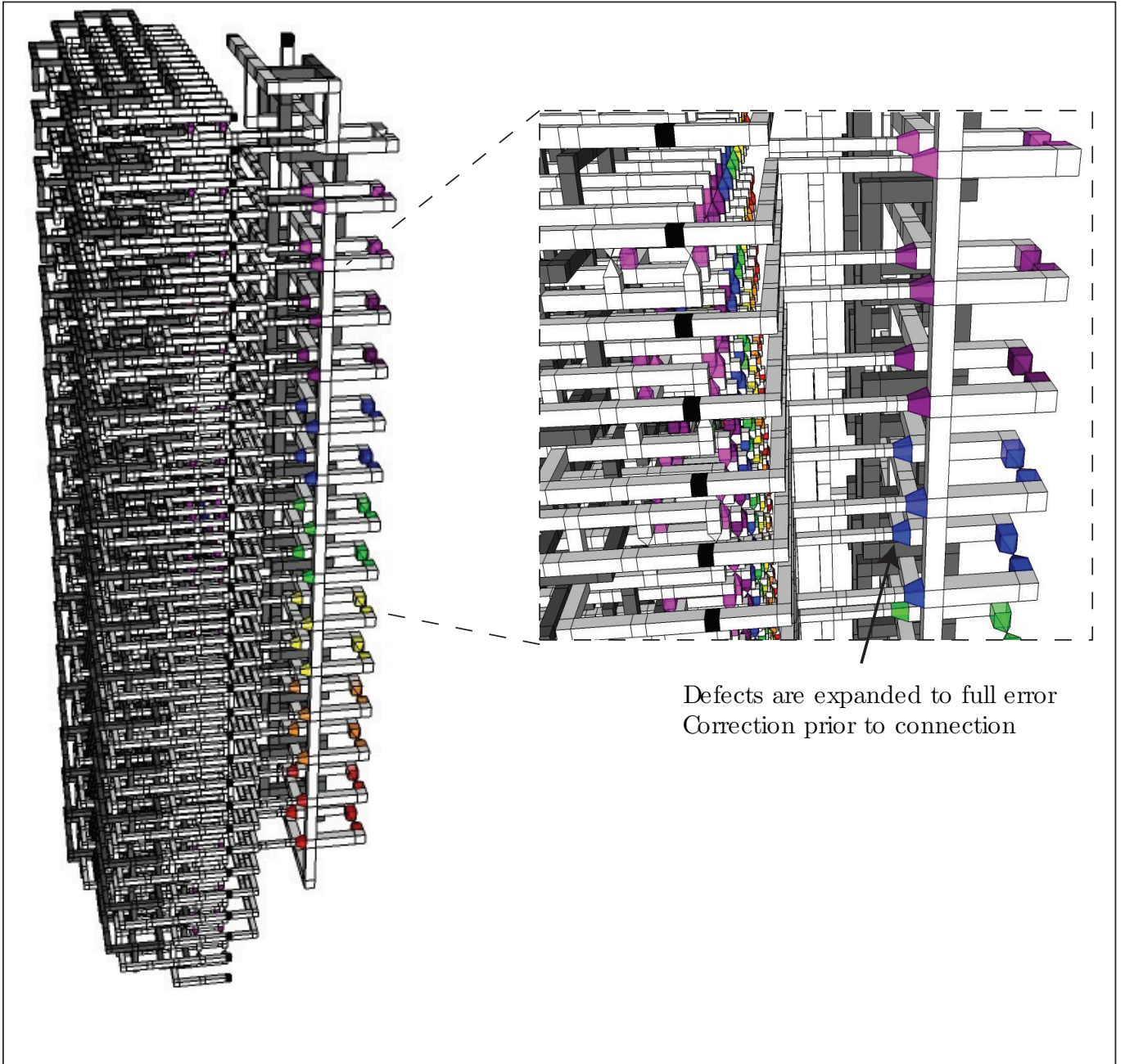


FIG. 15: Connecting multiple first level distillation circuits to the modified second level distillation circuit. Before the output of level one is connected to the relevant injection points at level two the defects are expanded to the full strength error correction needed at the algorithmic level. The first level distillation circuits can utilise a smaller error correcting code as the residual error from the distillation circuit will be higher than the required protection of the data qubits. As such, the first level defects must maintain a separation from the second level circuits compatible with the strength of error correction at level two.

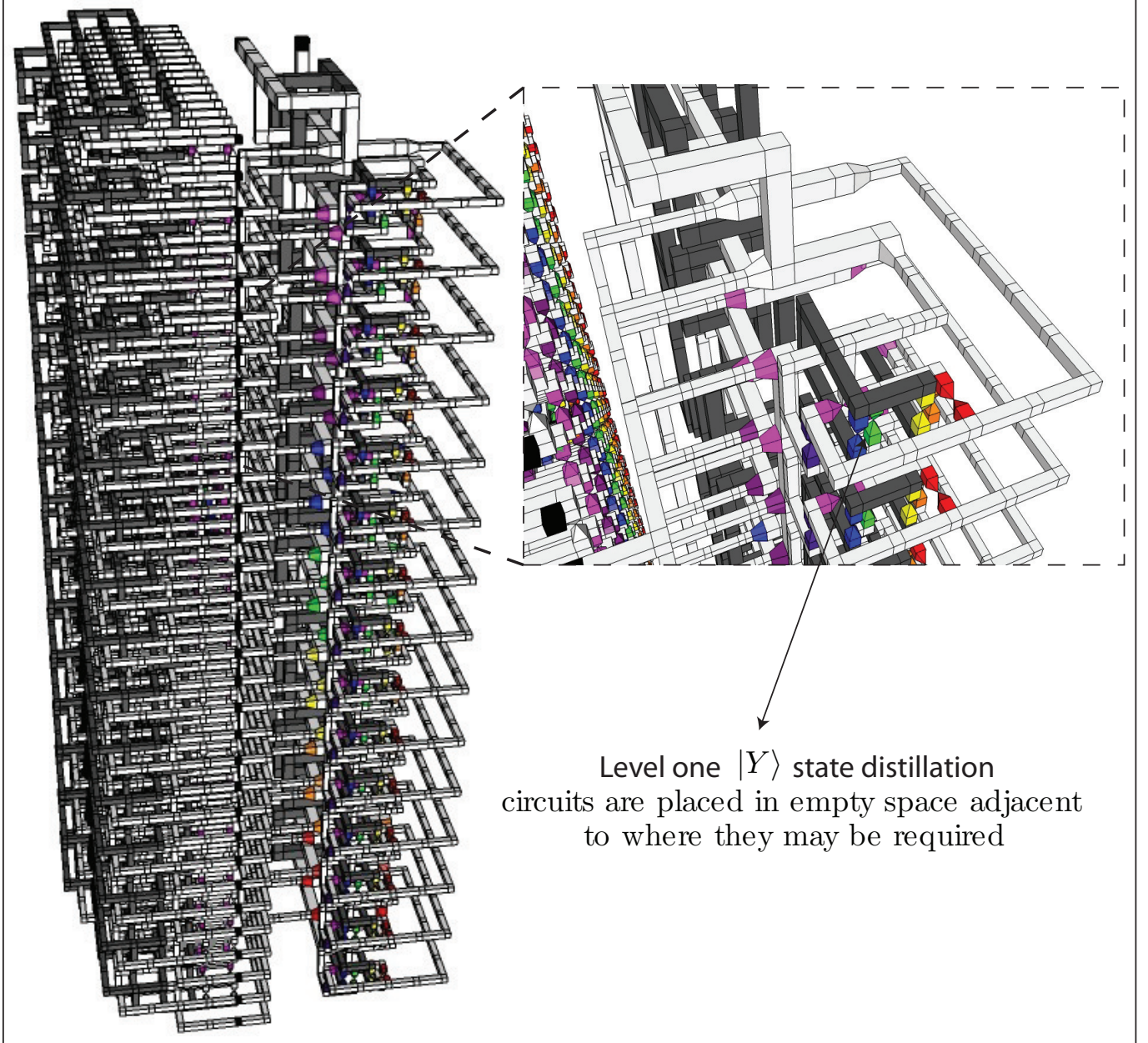


FIG. 16: 15 copies of level one $|Y\rangle$ state distillation are introduced into an empty cluster region to provide corrective operations to the $|A\rangle$ state distillation circuit at second level. These circuits can utilise smaller defects as they are level one circuits.

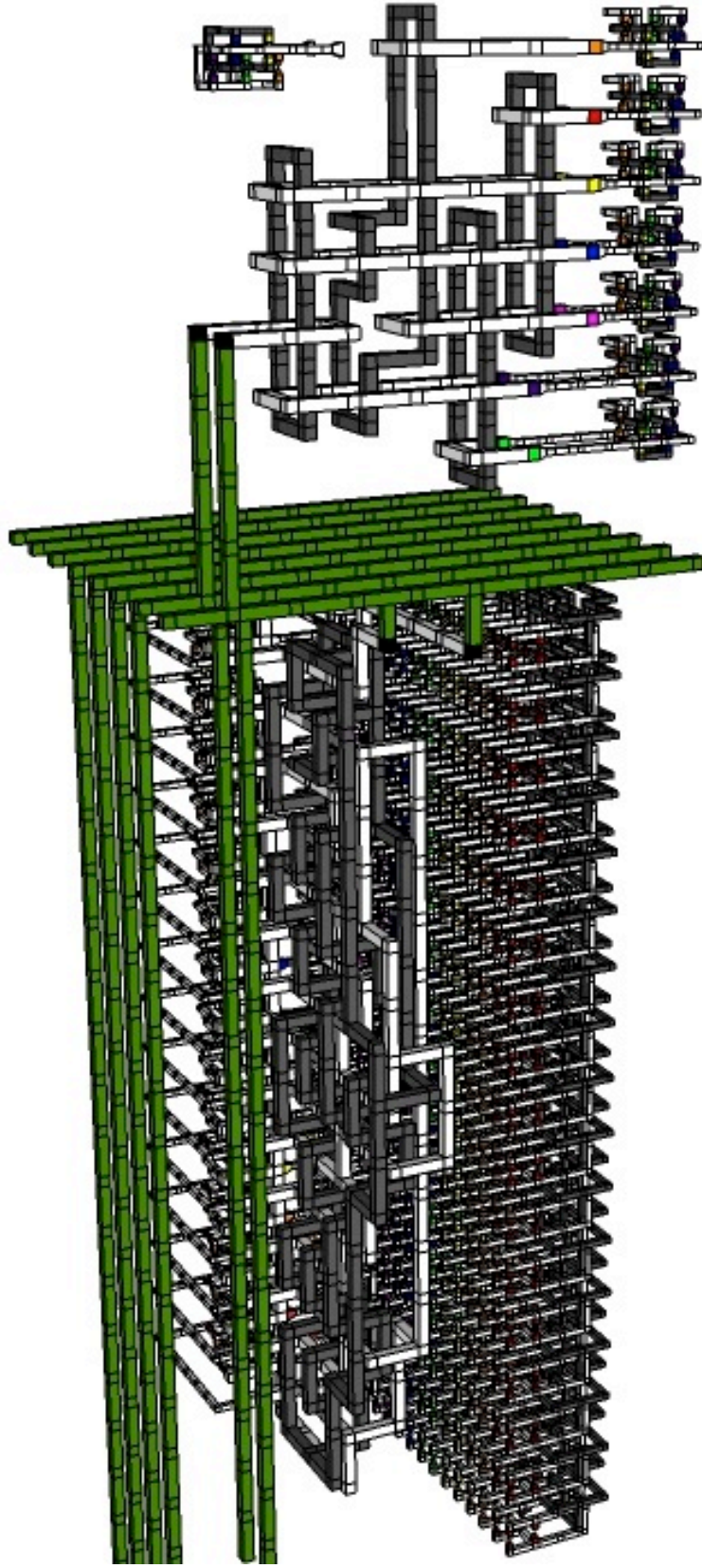


FIG. 17: Complete structure for the $R_z(\pi/8)$ rotation for one of the four algorithmic qubits present in the repeating unit (we have reversed the temporal axis in this image for readability). Two levels of $|A\rangle$ state distillation, with necessary correction gates sit below the algorithmic layer and two levels of $|Y\rangle$ state distillation exists above the algorithmic layer for the final $R_z(\pi/4)$ correction, required 50% of the time. There are additional redundant circuit elements that are included to protect against the failure of level one distillation circuits. The connection structures illustrated here assume no such failures occur. This circuit would have to be modified dynamically depending on the result of certain measurements.